Chapter 3

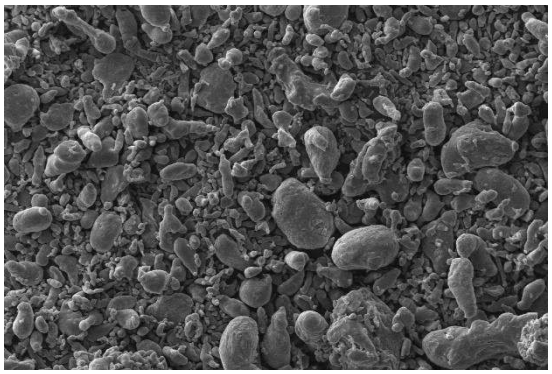

SYNTHESIS AND CHARACTERIZATION OF Al_3Zr/Al-Mg *insitu* COMPOSITES

3.1 Introduction

This chapter deals with the synthesis of Al_3Zr/Al-Mg composites with different vol.% of Al_3Zr particles by the direct melt reaction (DMR) *insitu* technique. The reaction between reactants was studied to find out the temperature of formation of Al_3Zr particles. The Al_3Zr/Al-Mg composites have been characterized by different techniques and the effect of different vol.% of Al_3Zr particles on microstructure, physical, mechanical and tribological properties of Al-Mg alloy is presented.

3.2 Fabrication of Al_3Zr/Al-Mg Composites

Al-Mg alloy was procured from Hindalco Industries Ltd, Renukoot, India and inorganic salt potassium hexa-fluro-zirconate (K_2ZrF_6) with 98.6% purity was obtained from Sigma Aldrich Chemicals Pvt. Ltd. Al-Mg alloy was analyzed by optical emission spectrometer which showed the presence of 2.26 wt.% magnesium and minor amount of other elements as 0.13 wt.% Si, 0.30 wt.% Fe, 0.01 wt.% Cu, 0.10 wt.% Mn, 0.18 wt.% Cr and the balance aluminium.

The composites were prepared by DMR technique (section 2.2). Based on stoichiometric ratio, required amount of inorganic salt for a particular composition was calculated (Table 3.1) [Li et al., 2007, 2009]. The required amount of K_2ZrF_6 powder corresponding to vol.% of reinforcement particles is given in Table 3.2. To prepare a composite with particular vol.% Al_3Zr, required amount (Table 3.2) of inorganic salt was dehydrated at 250°C for 3 hr and charged into Al-Mg melt at 885°C under argon atmosphere. The powder was mixed with the help of mechanical stirrer for 30 minute.

Five composites with different vol.% of Al_3Zr particle (10, 12.5, 15, 20 and 30 vol.%) were prepared. To calculate the actual vol.% of Al_3Zr particles formed, composites were analysed by optical emission spectrometer. The elemental analysis is given in Table 3.3, whereas theoretical and actual vol.% of Al_3Zr is given in Table 3.4 [Gautam and Mohan, 2016; Gautam et al., 2016a, 2016c].

Table 3.1 –Calculation for theoretical volume fraction of Al_3Zr particles in the composites.

Parameters	**Reactant**		**Product**
	13 Al	**3 K_2ZrF_6**	**3 Al_3Zr**
Molecular weight	351	849	516
Density (g/cc)	2.68		4.1
Amount of reactant and product (g)	If w is the total amount of alloy and x is the presumed amount of Al to react	(849x/351)w = 2.418xw	(516x/351)w = 1.47xw
Theoretical volume fraction	w/2.7		0.961x

Table 3.2 – Powder amount required for 0.5 kg Al-Mg alloy.

Composites	**K_2ZrF_6 powder (x10^{-3} Kg)**
10 vol.% Al_3Zr	125.81
12.5 vol.% Al_3Zr	157.26
15 vol.% Al_3Zr	188.71
20 vol.% Al_3Zr	251.61
30 vol.% Al_3Zr	377.42

Table 3.3 – Chemical compositions of as cast composites.

Element	Si	Fe	Cu	Mn	Mg	Cr	Zn	Zr	Al
10 vol.%Al_3Zr	0.11	0.32	0.04	0.08	2.24	0.16	0.06	19.75	Bal.
12.5 vol.%Al_3Zr	0.10	0.33	0.01	0.09	2.23	0.15	0.05	24.37	Bal.
15 vol.%Al_3Zr	0.12	0.30	0.03	0.10	2.20	0.16	0.04	28.94	Bal.
20 vol.%Al_3Zr	0.14	0.32	0.01	0.09	2.19	0.18	0.05	38.67	Bal.
30 vol.%Al_3Zr	0.13	0.30	0.02	0.10	2.16	0.17	0.04	57.75	Bal.

Table 3.4 – Theoretical and actual vol.% of Al_3Zr in composites.

Composites	vol.% Al_3Zr	
	Theoretical	Actual
10 vol.% Al_3Zr	10	9.07
12.5 vol.% Al_3Zr	12.5	11.19
15 vol.% Al_3Zr	15	13.28
20 vol.% Al_3Zr	20	17.75
30 vol.% Al_3Zr	30	26.51

3.3 XRD and DTA Analysis

XRD curves of composites superimposed with XRD of base alloy are shown in Fig. 3.1. The diffraction peaks observed in this figure correspond to Al_3Zr and Al phases only which confirms formation of Al_3Zr particles. It is also observed that intensity of Al_3Zr peaks increases with their vol.%. The chemical reaction between molten aluminium alloy and inorganic salt K_2ZrF_6 at 885°C forming Al_3Zr intermetallic particles is given in following equations:

$$3K_2ZrF_6 + 4Al_{(l)} = 4AlF_{3(g)} + 6KF_{(g)} + 3[Zr] \quad (3.1)$$

The reduced zirconium reacts with liquid aluminium to form Al_3Zr particles according to the eqn. (3.2):

$$3Al_{(l)} + [Zr] = Al_3Zr \quad (3.2)$$

Therefore, the final reaction can be given as,

$$3K_2ZrF_6 + 13Al_{(l)} = 3Al_3Zr + 4AlF_{3(g)} + 6KF_{(g)} \quad (3.3)$$

The ΔG^{Θ} value for Al_3Zr phase has been reported as [Li et al., 2007, 2009]:

$$\Delta G^{\Theta}_{ZrAl_3} = -25138.3 - 319.4T \quad (3.4)$$

The first peak in DTA curve (Fig. 3.2) corresponds to endothermic reaction (melting of Al-Mg alloy) at about 661.2°C while second peak at 885.7°C corresponds to the exothermic reaction (formation of Al_3Zr). The negative value of ΔG^{Θ} (-395.22 kJ) from eqn. (3.4) at 885.7°C indicates that Al_3Zr phase is stable at this temperature. AlF_3 and KF are the gaseous compounds which partially go out of the melt during reaction of molten aluminium alloy with K_2ZrF_6 powder and the residual is degassed by terta-chloro-ethane. XRD pattern of the composites doesn't show any peak other than aluminium and Al_3Zr intermetallic, which confirms the completion of chemical reaction. For secondary confirmation Al_3Zr particles were extracted by immersing the as cast composites in 10% HCl solution for several days [Zhen and Davies, 1983]. XRD analysis of extracted particles (Fig. 3.3) shows the presence of only Al_3Zr particles (Fig. 3.4) [Gautam and Mohan, 2016; Gautam et al., 2016a, 2016c].

3.4 Physical Properties

Theoretical and experimental densities (evaluated by Archimedes principle) of Al-Mg alloy and composites are given in Table 3.5. Density increases with increase in amount of Al_3Zr particles. The porosity values are also reported in this table and are within a range of 5 to 7 vol.%.

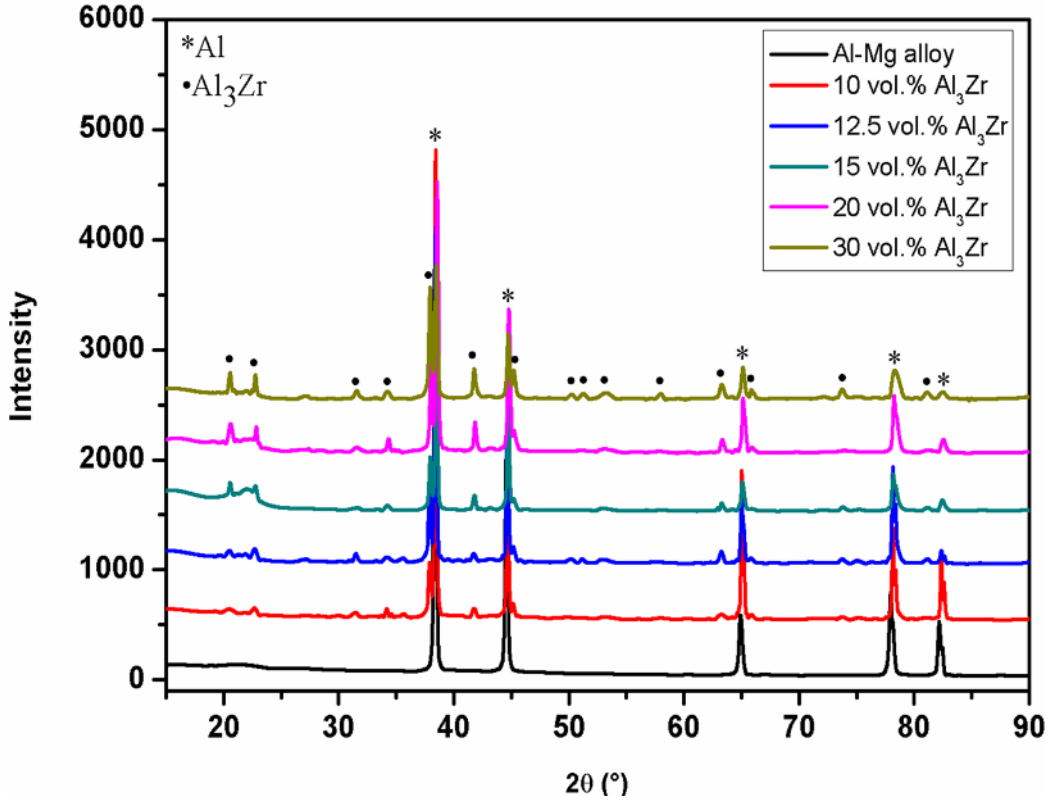

Figure 3.1 – XRD pattern of Al-Mg alloy and composites [Gautam and Mohan, 2016; Gautam et al., 2016a, 2016c].

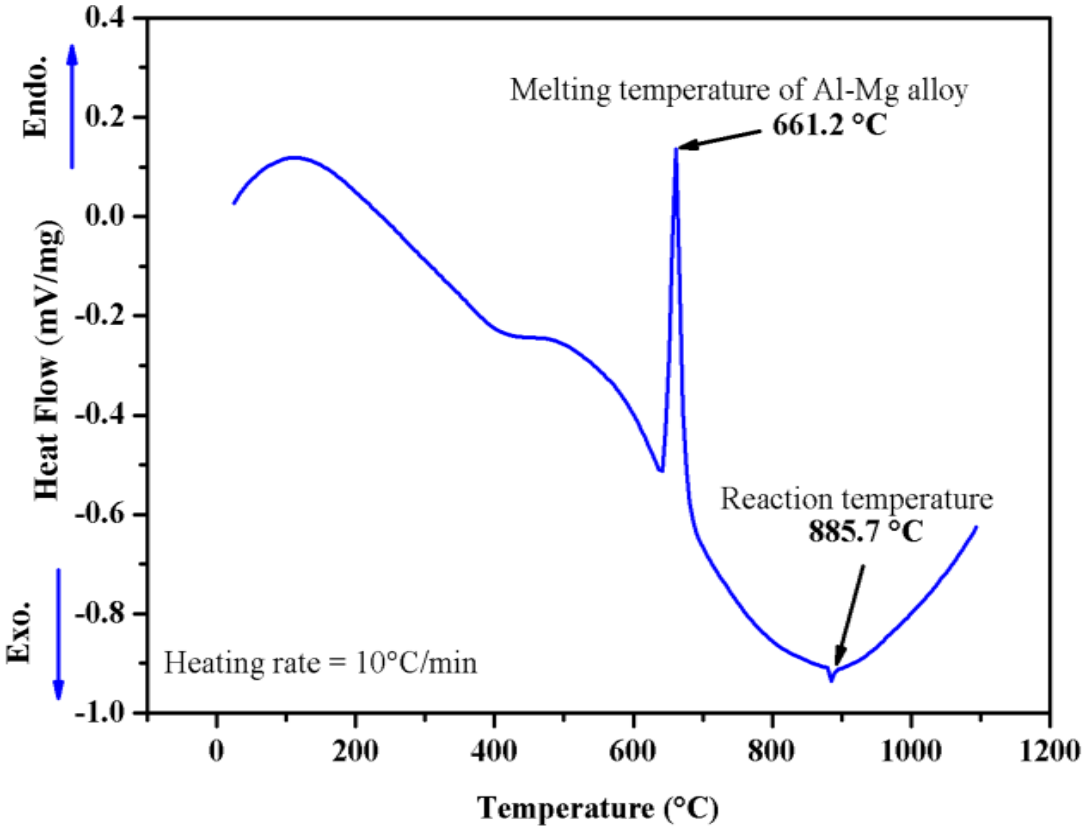

Figure 3.2 – DTA curve of Al_3Zr/Al-Mg composite [Gautam et al., 2016c].

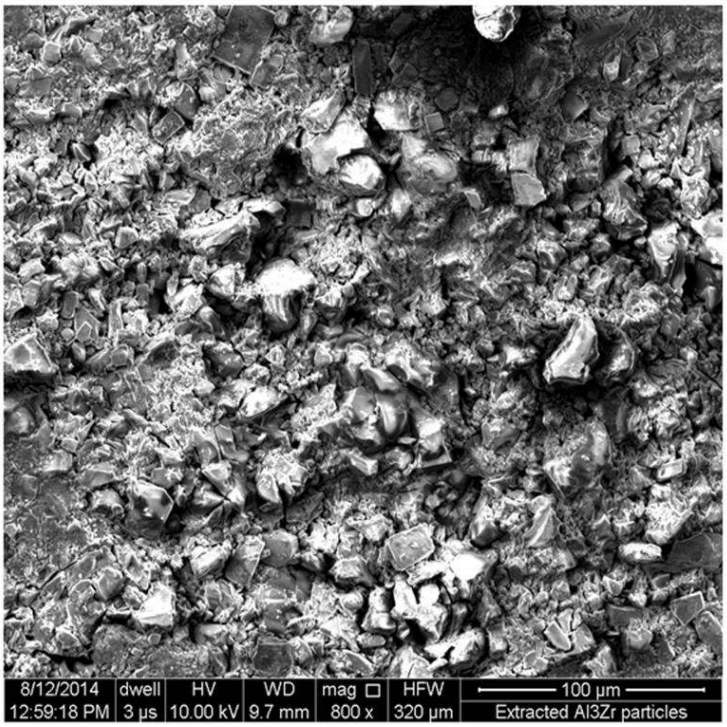

Figure 3.3 – SEM micrograph of extracted particles [Gautam et al., 2016c].

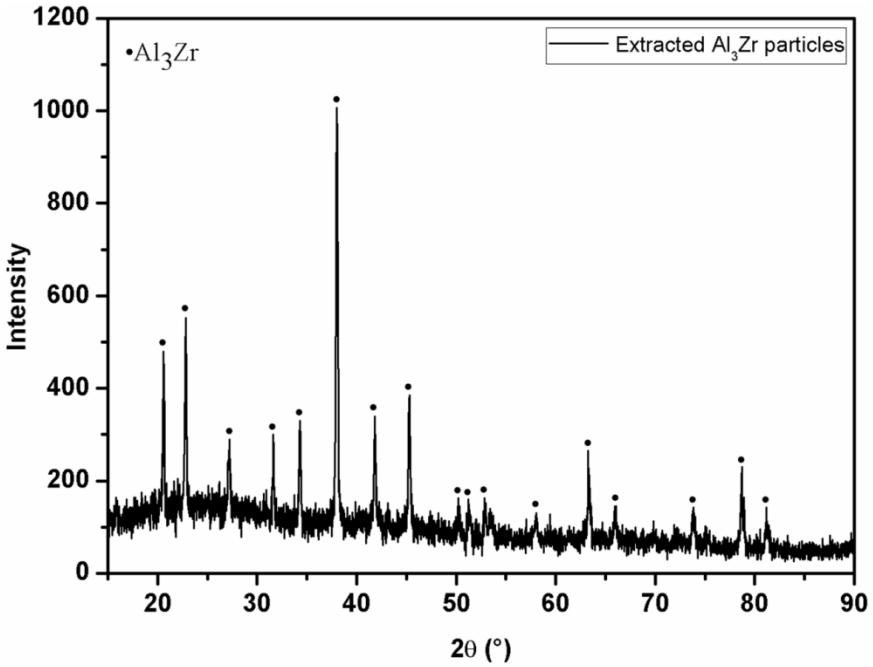

Figure 3.4 – XRD pattern of extracted particles from Al_3Zr/Al-Mg composite [Gautam et al., 2016c].

Table 3.5 – Density and porosity of Al-Mg alloy and composites [Gautam and Mohan, 2016; Gautam et al., 2016c].

Materials	Density, Kg/m^3 (x10^3)		Porosity (vol.%)
	Theoretical	Experimental	
Al-Mg alloy	2.68	2.50	7.00
10 vol.% Al_3Zr	2.82	2.66	5.74
12.5 vol.% Al_3Zr	2.86	2.69	5.99
15 vol.% Al_3Zr	2.89	2.70	6.79
20 vol.% Al_3Zr	2.97	2.79	6.06
30 vol.% Al_3Zr	3.11	2.93	5.67

3.5 Optical Microscopy

Optical micrographs of Al-Mg alloy and Al_3Zr/Al-Mg composites with different vol.% of Al_3Zr particles are shown in Fig. 3.5a-f. Al_3Zr particles appear as black patches in optical micrographs. These regions increase with increasing vol.% of Al_3Zr particles. This figure shows refinement of Al-rich grains with *insitu* formation of Al_3Zr particles (Fig. 3.5a-b) and this phenomenon increases with increase in Al_3Zr particles (Fig. 3.5b-f). The grain size for Al-Mg matrix alloy and composites with different vol.% of Al_3Zr particles has also been evaluated and values are given in Table 3.6. Phenomenon of grain refinement becomes further clear with grain size values given in this table.

Polyhedral Al_3Zr particles work as a catalyst for the heterogeneous nucleation of Al-rich phase and this phenomenon is pronounced with increasing amount of Al_3Zr. Further, 0.95% lattice misfit between aluminium and Al_3Zr particles also contributes in refinement of Al-rich grains. Ebrahimi et al. [2010] and Zhao et al. [2003] also observed grain refinement in different Al alloy matrices in the presence of Al_3Zr particles [Gautam and Mohan, 2016; Gautam et al., 2016a, 2016c].

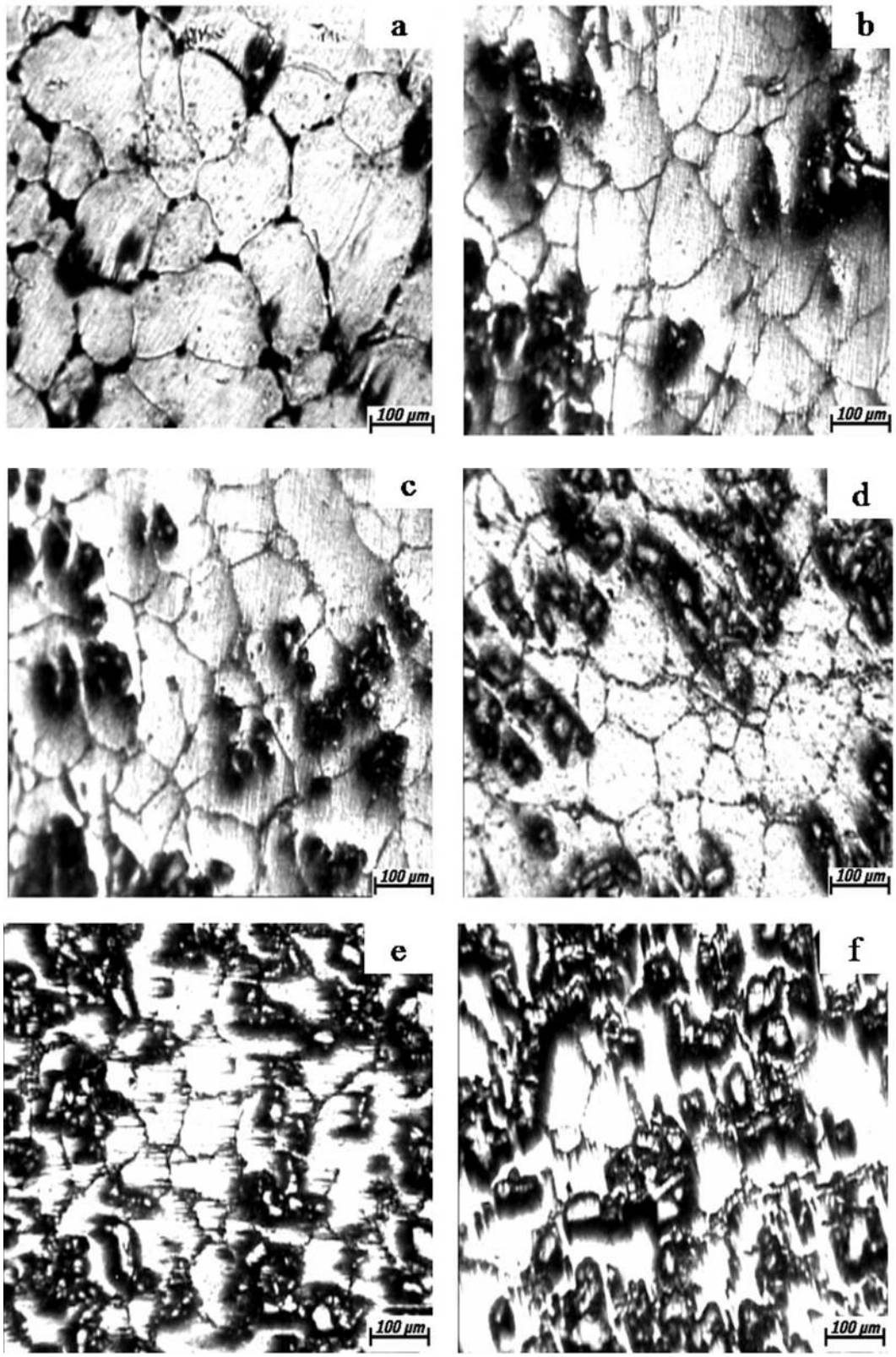

Figure 3.5 – Optical micrographs of (a) Al-Mg alloy, and composites with (b) 10 vol.% Al_3Zr, (c) 12.5 vol.% Al_3Zr, (d) 15 vol.% Al_3Zr, (e) 20 vol.% Al_3Zr, and (f) 30 vol.% A_3Zr.

Table 3.6 – The values of grain size in Al-Mg alloy and composites.

Materials	**Average grain size (µm)**
Al-Mg alloy	129.56
10 vol.% Al_3Zr	105.50
12.5 vol.% Al_3Zr	98.35
15 vol.% Al_3Zr	80.25
20 vol.% Al_3Zr	74.33
30 vol.% Al_3Zr	-

3.6 Electron Microscopy

Electron microscopic studies of composite materials were conducted to have clarity in morphology and distribution of Al_3Zr particles. SEM micrographs in Fig. 3.6 show uniform distribution of *insitu* formed Al_3Zr particles in Al-rich matrix for all composites with different vol.% of Al_3Zr particles. SEM micrographs (Fig. 3.7a-b) also show rectangular and polyhedron Al_3Zr particles. Zhao et al. [2003] and Kaveendran et al. [2013] also observed different morphologies of Al_3Zr particles in different matrices and according to Zhao et al. [2003] it could be due to twinning effect. EDS analysis of Al_3Zr particle in Fig. 3.7c shows the presence of only aluminium and zirconium which further confirms the *insitu* formation of only Al_3Zr particles. Figure 3.8 shows the Al_3Zr particle size histogram. More than seven hundred readings of Al_3Zr particles were taken to illustrate the particle size histogram and it indicates that Al_3Zr particles are mostly within a size range of 5 to 19 µm.

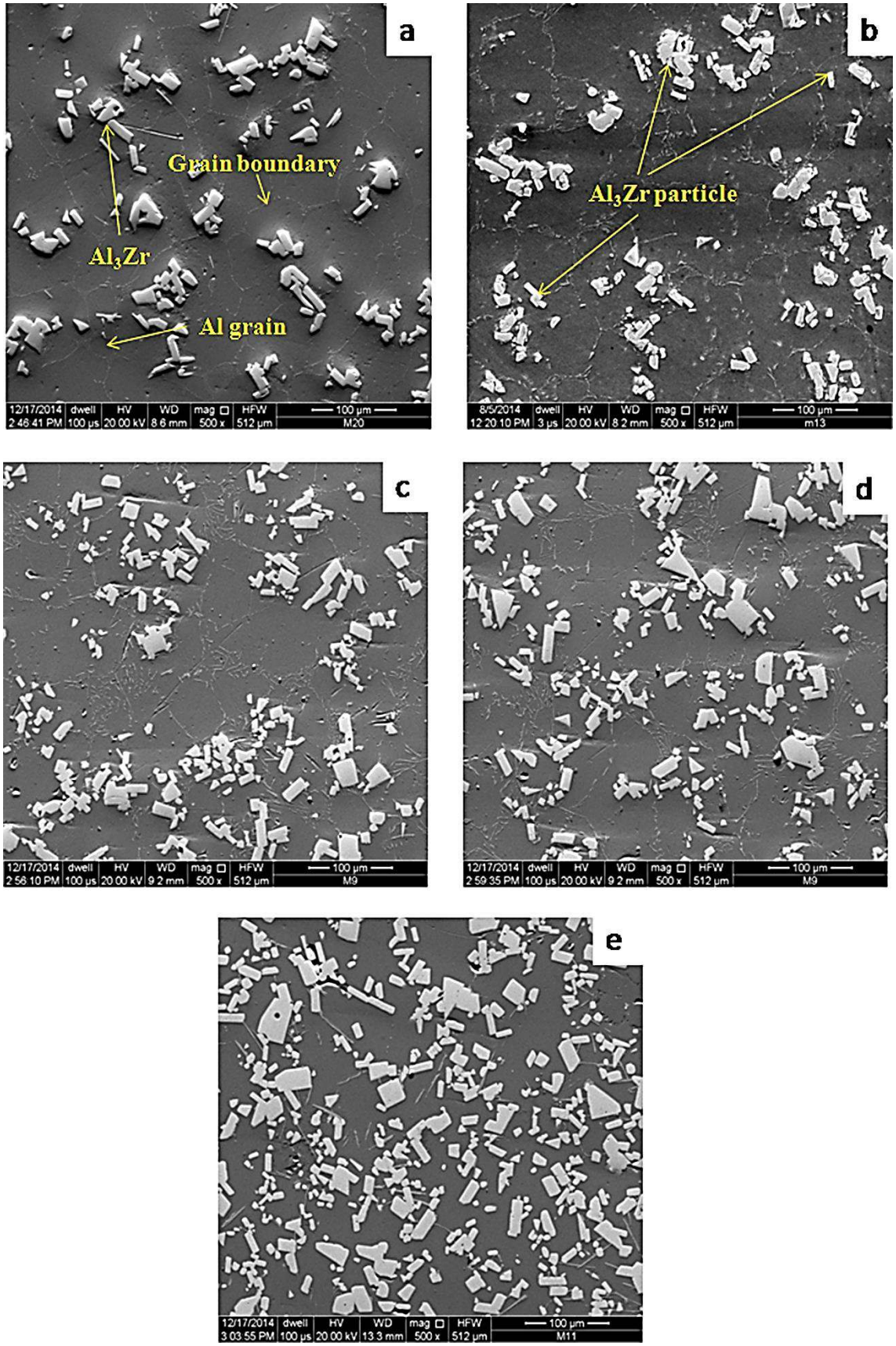

Figure 3.6 – Scanning electron micrographs of composites with different vol.% of Al_3Zr particles (a) 10 vol.% Al_3Zr, (b) 12.5 vol.% Al_3Zr, (c) 15 vol.% Al_3Zr, (d) 20 vol.% Al_3Zr, and (e) 30 vol.% A_3Zr.

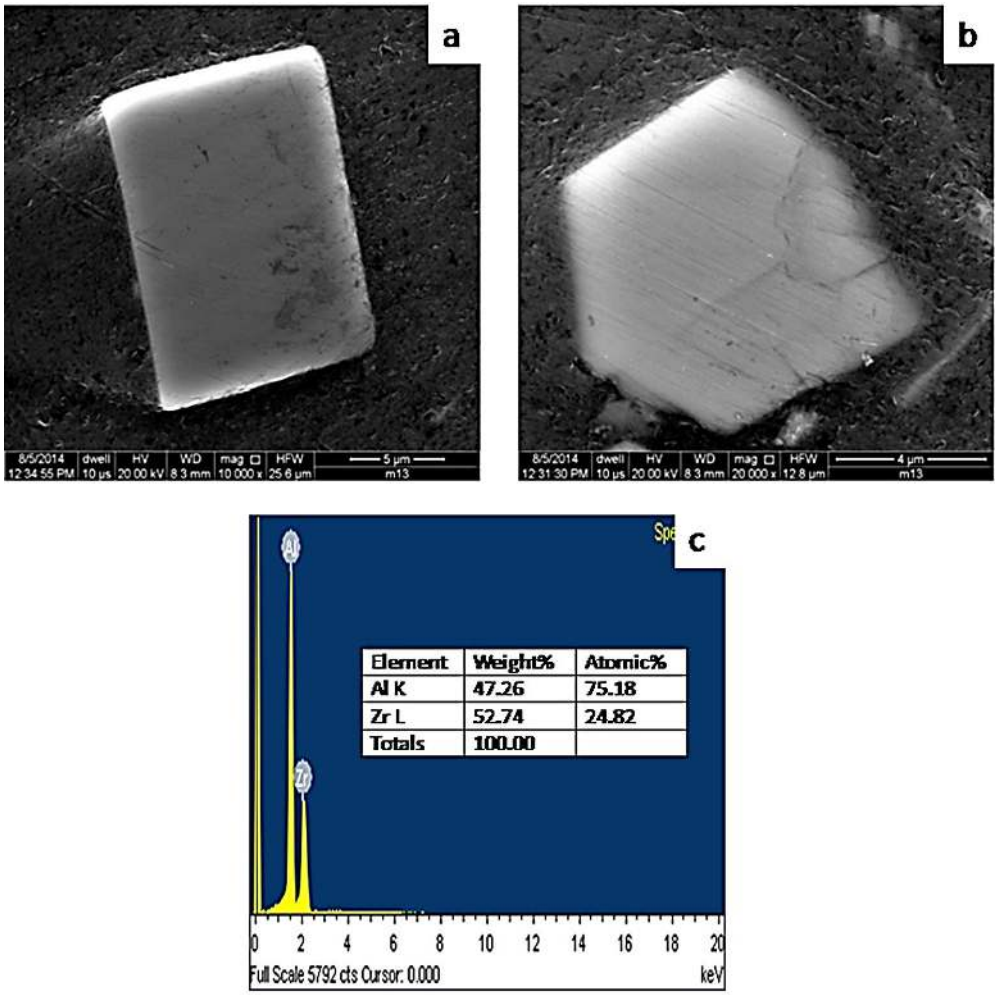

Figure 3.7 – Scanning electron micrographs of (a) rectangular Al_3Zr, (b) polyhedron Al_3Zr, and (c) EDS of theAl_3Zr [Gautam and Mohan, 2016; Gautam et al., 2016c].

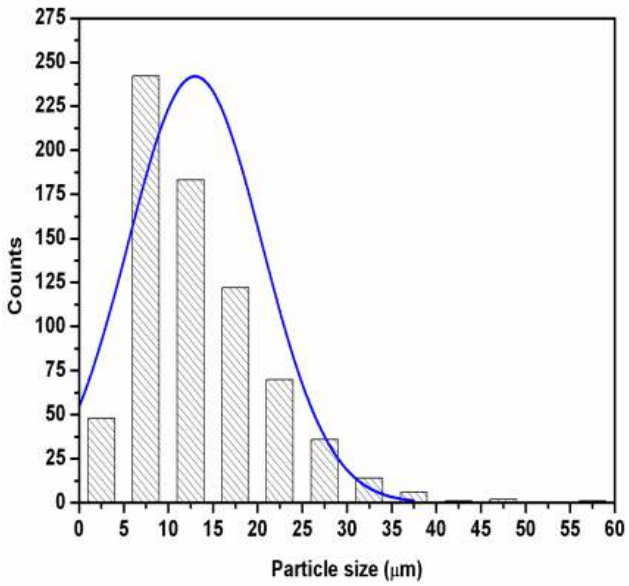

Figure 3.8 – Histogram showing of particle size distribution of Al_3Zr particles in composites [Gautam et al., 2016c].

TEM micrograph in Fig. 3.9a shows the rod-like structure of Al_3Zr particle (not observed in SEM studies) with length/diameter (L/D) ratio of 4.2. The SAD pattern (Fig. 3.9b) of Al_3Zr particle shows that it has body centered tetragonal (BCT) structure with space group I_4/mmm, while SAD of matrix confirms that it has face centered cubic (fcc) structure (Fig. 3.9c). Figure 3.9d shows presence of dislocations near rod like Al_3Zr particles. These dislocations could be resulted during synthesis of composite due to the mismatch in coefficient of thermal expansion of matrix and particles. Zhao et al. [2008] also observed same phenomenon in *insitu* formation of $(Al_2O_3+Al_3Zr)$/Al nano-composites synthesized by magneto-chemical melt reaction technique [Gautam and Mohan, 2016; Gautam et al., 2016a, 2016c].

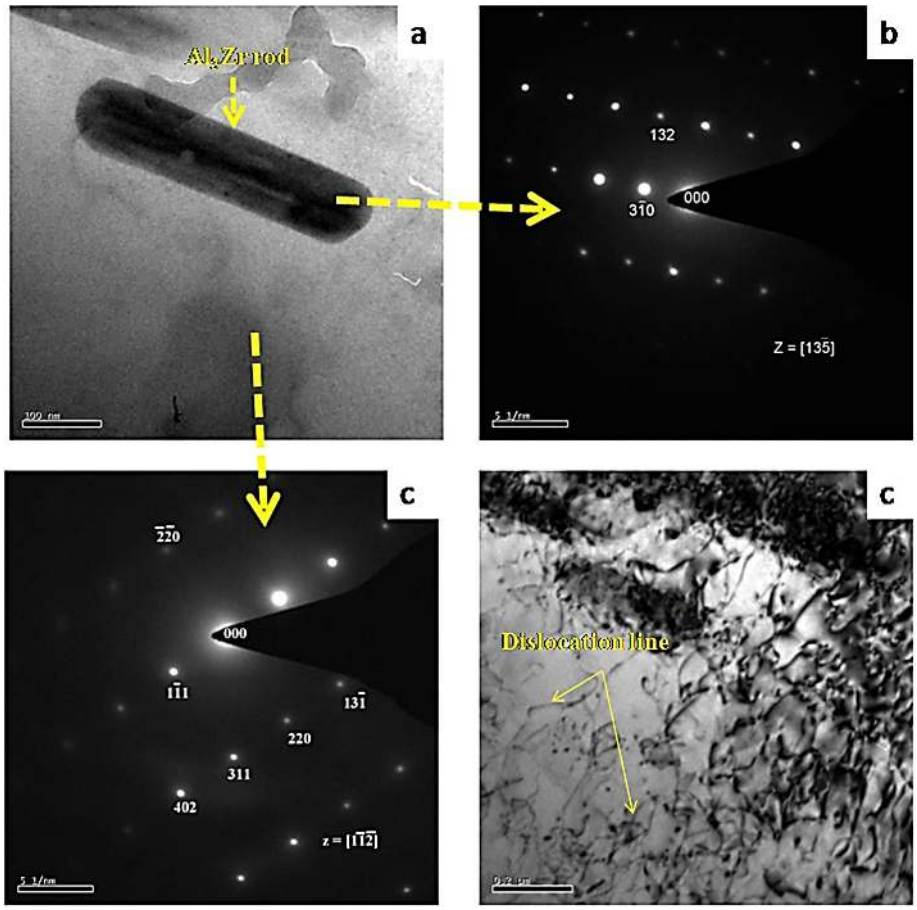

Figure 3.9 – TEM Micrographs of Al_3Zr/Al-Mg composite: (a) showing the rod like Al_3Zr particle, (b) SAD pattern of the rod like Al_3Zr, (c) SAD pattern of matrix, and (d) dislocation near rod like Al_3Zr particle [Gautam et al., 2016c].

3.7 Mechanical Properties and Fractography

Figure 3.10 shows ambient temperature engineering stress-strain curves of as cast Al-Mg alloy and composites with different vol.% of Al_3Zr particles. These curves have been used to evaluate ultimate tensile strength (UTS), yield strength (YS) and percentage elongation of different compositions. Data of UTS, YS, % elongation and hardness is given in Table 3.7 and has been plotted in Fig. 3.11. All properties show an increase with increasing vol.% of Al_3Zr particles up to 15 vol.%, but with further addition of Al_3Zr (i.e. 20 and 30 vol.%) all values decrease. However, UTS and YS of composites with 20 & 30 vol.% Al_3Zr still remain higher than that of base alloy, but value of % elongation falls below even that of base alloy for 30 vol.% of Al_3Zr. Strengthening in these composites takes place due to refining of matrix phase (Fig. 3.5) and formation of dislocations (Fig. 3.9d).

Fracture study shows that inclusion of Al_3Zr particles in Al-Mg alloy changes the mode of fracture from quasi-cleavage to ductile with larger dimples (Fig. 3.12a-b). Composite with 10 vol.% Al_3Zr particles (Fig. 3.12b) shows large dimples and facets of Al_3Zr particles on the surface resulting in ductile fracture. The polyhedral Al_3Zr particles work as a catalyst for heterogeneous nucleation of Al-rich phase (matrix phase) and strengthening effect increases with increasing vol.% of polyhedral shape Al_3Zr particles. Dislocations near the rod like structure of Al_3Zr particle (Fig. 3.9d) are observed due to a mismatch of the coefficient of thermal expansion (CTE) between the matrix and reinforcement which also contribute to the improvement in strength of the composites. At higher compositions, cracks are initiated either at the particle-matrix interface or within the harder particle itself causing decrease in dimple size, and

combined mode of fracture is observed. With increase in vol.% of Al_3Zr particles brittle mode of fracture dominates and the ductility reduces (Fig. 3.12c-f) causing the early failure.

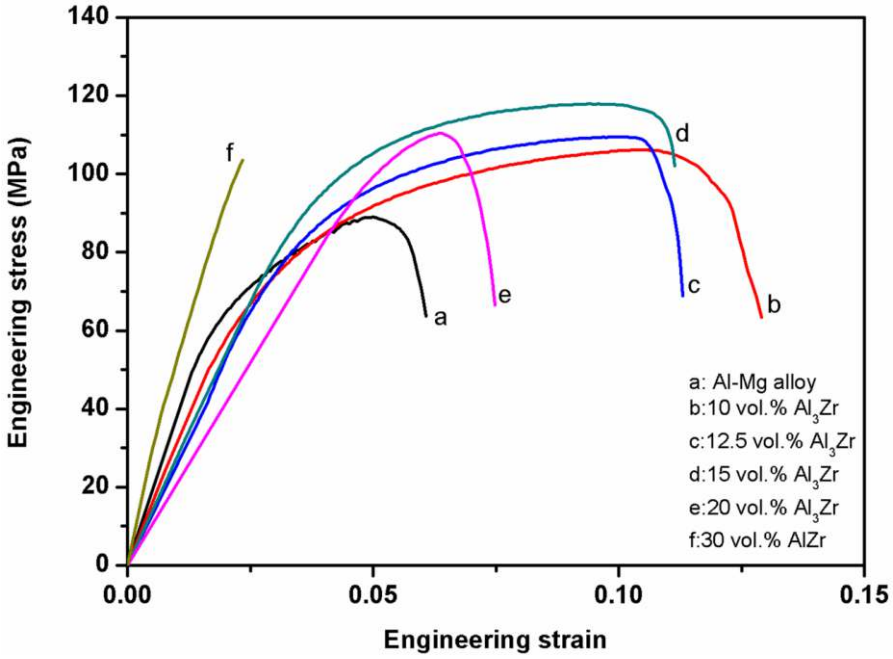

Figure 3.10 – Engineering stress-strain curves of the Al-Mg alloy and composites.

Table 3.7 – Summarized data of mechanical properties in Al-Mg alloy and composites.

Vol.% of Al_3Zr	Strength parameters (MPa)		(%) Elongation	Bulk Hardness (BHN)
	UTS	YS		
0	89.0	59.0	6.08	28.47
10	106.2	64.4	12.88	35.00
12.5	110.0	78.1	11.50	37.32
15	118.5	84.6	11.00	39.43
20	110.5	69.2	7.50	43.20
30	103.6	66.5	2.40	52.00

Improvement in percentage elongation (Fig. 3.11) at 10 vol.% Al_3Zr may be attributed to the grain refining effect of the Al_3Zr particles. The enhanced resistance to the crack propagation due to grain refinement could have led to the improvement in the fracture

toughness and ductility as also observed by Tian et al. [2014] in case of 2024 Al alloy reinforced with ZrB_2 particles. However, at higher compositions early failure is caused due to larger crack nucleation sites which results in poor ductility and toughness.

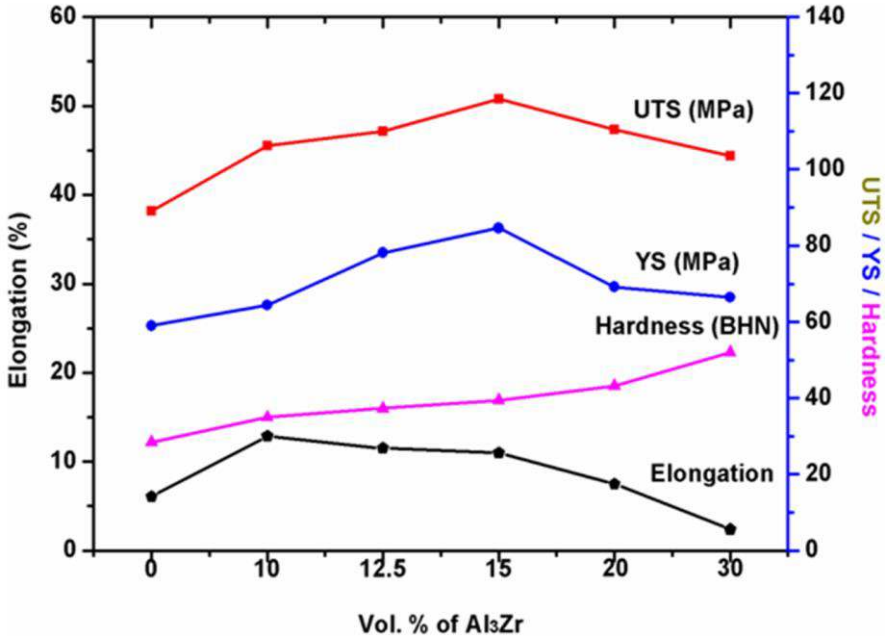

Figure 3.11 – Variation of mechanical properties in composites.

Figure 3.11 also shows variation in Brinell hardness with vol.% Al_3Zr particles. Hardness increases continuously with increase in vol.% of Al_3Zr particles. Hard Al_3Zr particles are the main cause of higher hardness, however, dislocations (Fig. 3.9d) and refining of matrix (Fig. 3.5) also contribute to hardness. Dislocations increase with increase in the vol.% of Al_3Zr particles and act as an obstacle to plastic deformation which enhances the hardness of matrix and contribute to overall hardness of the composites. Maximum hardness has been observed for composite with 30 vol.% of Al_3Zr particles and it is almost 85% higher than that of base alloy. Kumar et al. [2013] also observed same behaviour of hardness in AA6061 *insitu* composites reinforced with Al_3Zr particles [Gautam and Mohan, 2016; Gautam et al., 2016a, 2016c].

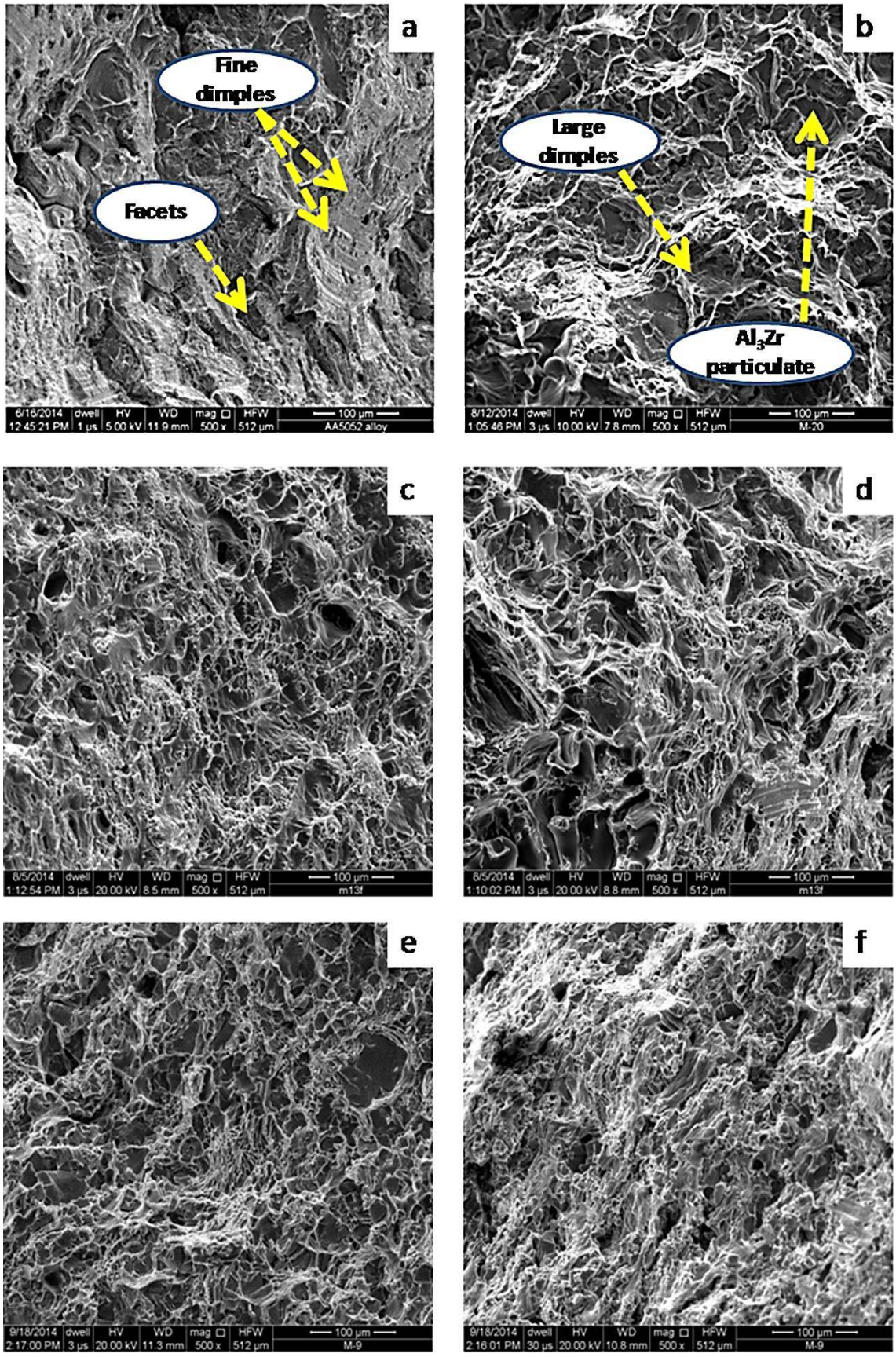

Figure 3.12 – Fractographs of (a) Al-Mg alloy, and composites with (b) 10 vol.% Al_3Zr, (c) 12.5 vol.% Al_3Zr, (d) 15 vol.% Al_3Zr, (e) 20 vol.% Al_3Zr, (f) 30 vol.% Al_3Zr.

3.8 Tribological Properties

Wear and friction results at different distance slid, loads, sliding velocities and compositions are presented in subsequent sub-sections. Worn surface studies under SEM & 3D – Profilometer and debris analysis have been used to analyse the results.

3.8.1 Effect of Sliding Distance

Figure 3.13a-b shows the variation of cumulative mass loss and coefficient of friction with sliding distance for Al-Mg alloy and composites at 1 m/s sliding velocity. Figure 3.13a shows that the cumulative wear increases linearly for all compositions with distance slid, whereas, coefficient of friction shows a fluctuating tendency about a mean value within a limit of ±0.025 for all compositions with distance slid (Fig. 3.13b).

3.8.2 Effect of Load

Figure 3.14a-c shows the variation of wear rate, wear rate per unit vol.% of Al_3Zr particles and coefficient of friction with load for all compositions at 1 m/s sliding velocity. Wear rate and wear rate per unit vol.% of Al_3Zr particles continuously increase with increase in load for all compositions, but after 30 N load the rate of increase is more, whereas, coefficient of friction with load shows completely reverse trend.

3.8.3 Effect of Sliding Velocity

Figure 3.15a-c show the variation of wear rate, wear coefficient and coefficient of friction with sliding velocity for all compositions at 20 N normal load. Wear rate of base alloy and 10, 12.5 and 15 vol.% Al_3Zr composites initially decreases and attains a minimum value at 3 m/s sliding velocity, and then increases sharply with further increase in sliding velocity.

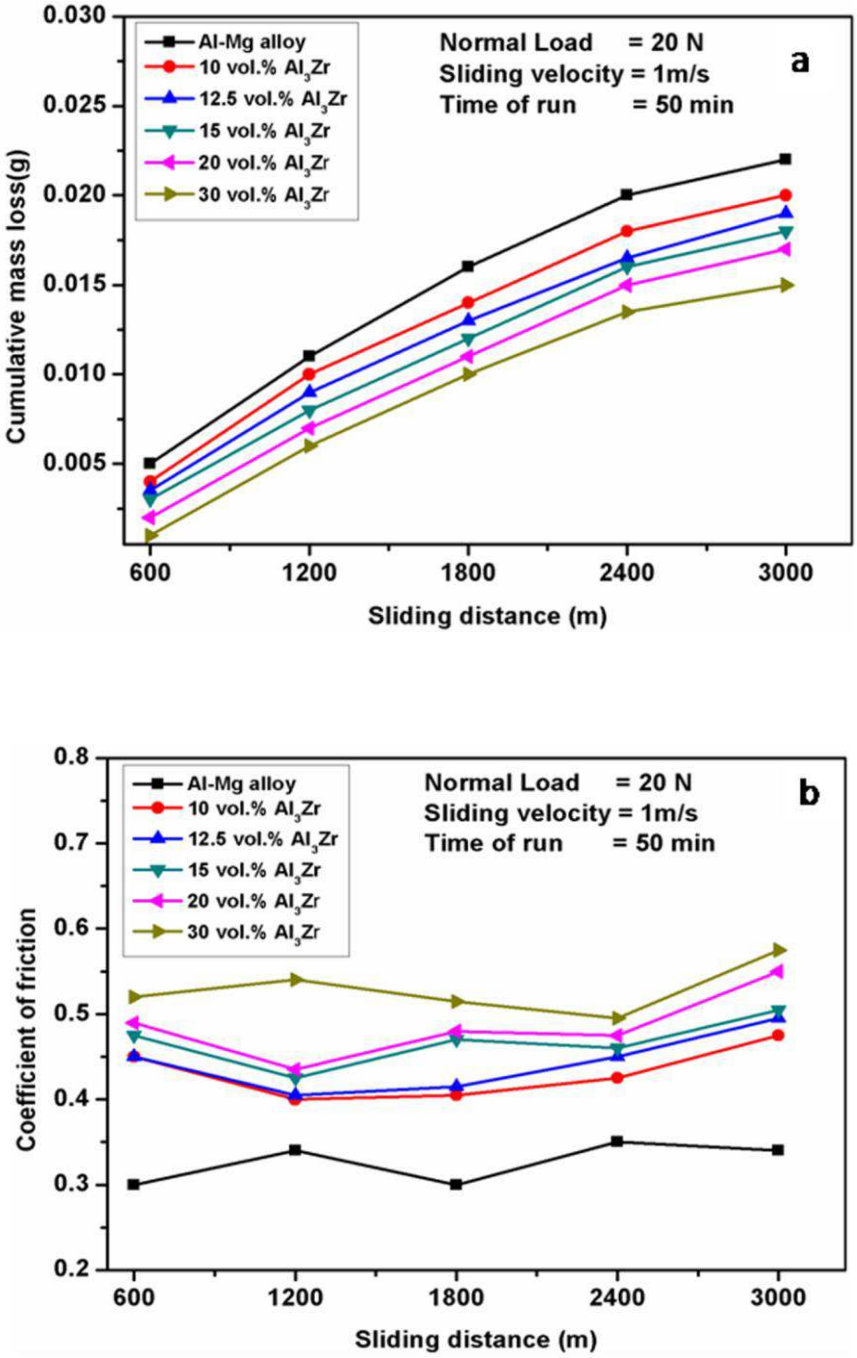

Figure 3.13 – (a) Variation of cumulative mass loss with sliding distance, and (b) coefficient of friction with sliding distance.

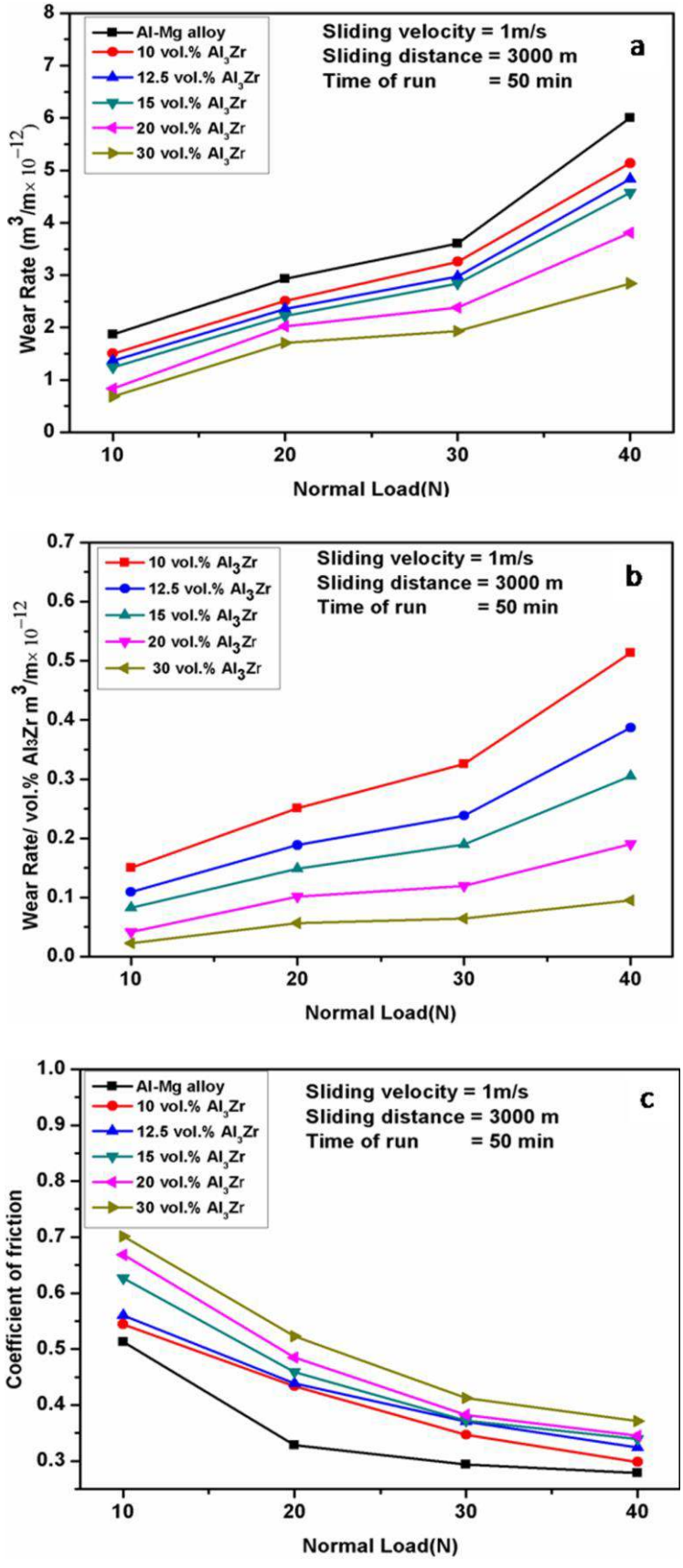

Figure 3.14 – (a) Variation of wear rate with normal load, (b) wear rate/ vol.% Al_3Zr with normal load, and (c) coefficient of friction with normal load.

But wear rate of composites with 20 and 30 vol.% Al_3Zr particles continuously increases (Fig. 3.15a). Further, it is also noted that at high sliding velocity, wear rate of these composites is much lower than the wear rate of base alloy and composites with 10, 12.5 and 15 vol.% Al_3Zr particles. Wear coefficient is defined as the volume of material loss per unit normal load and per unit sliding distance. It presents the load bearing capacity of the material. Wear coefficient versus sliding velocity also follows the same trend (Fig. 3.15b) as observed for wear rate. It is observed from Fig. 3.15c that coefficient of friction increases with sliding velocity for all compositions.

3.8.4 Effect of Composition

Figure 3.16a-d shows the variation of wear rate, normalized wear rate, wear coefficient and coefficient of friction with vol.% Al_3Zr particles. Normalized wear rate has been defined as the wear rate of composites per unit wear rate of base alloy. It is observed from these figures that wear rate, normalized wear rate and wear coefficient all decrease with increasing amount of Al_3Zr particles, whereas, coefficient of friction increases continuously with an increasing amount of Al_3Zr.

3.8.5 Worn Surface Topography and Mechanism

Wear and friction behaviour of materials depend on several factors such as their morphology, mechanical properties, surface conditions prior to test and operating parameters. Surface studies under SEM and Profilometer after test help to analyse the wear and friction results. Nature of debris also helps to understand the wear mechanism. Line analysis and 3D image under Profilometer of a polished wear specimen is shown in Fig. 3.17. Surface is quite smooth as evident from 3D image and its R_a value is 0.389μm.

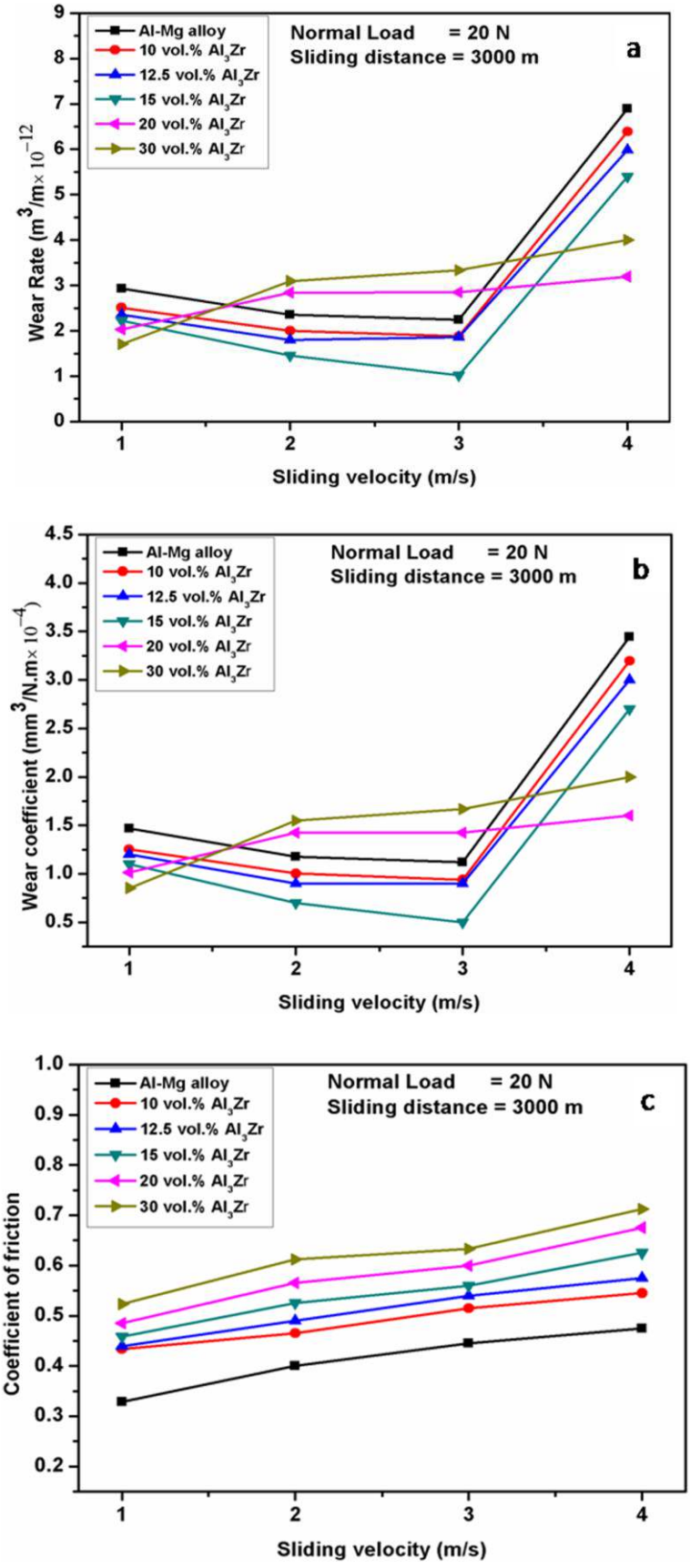

Figure 3.15 – (a) Variation of wear rate with sliding velocity, (b) wear coefficient with sliding velocity, and (c) coefficient of friction with sliding velocity.

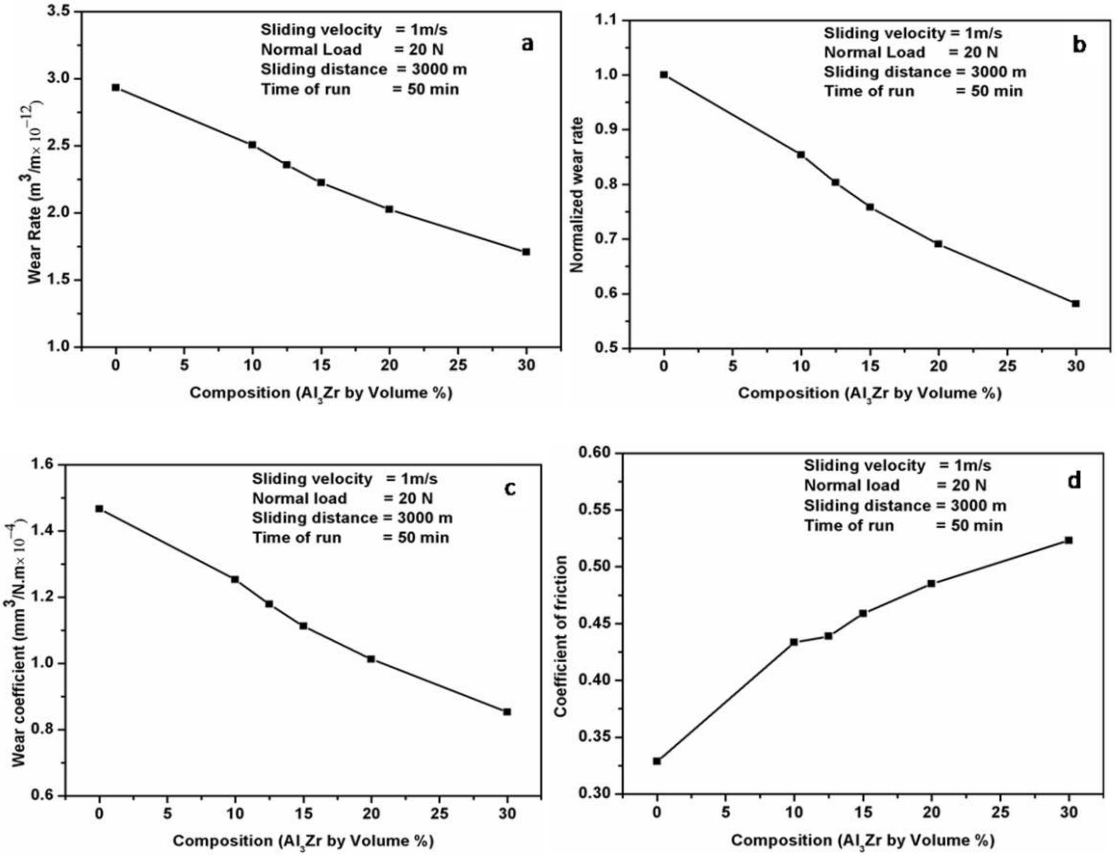

Figure 3.16 – (a) Variation of wear rate with vol.% of Al_3Zr, (b) normalized wear rate with vol.% of Al_3Zr, (c) wear coefficient with vol.% of Al_3Zr; and (d) coefficient of friction with vol.% of Al_3Zr.

When base alloy and composites are subjected to wear and friction test, quite linear increase in cumulative wear is observed with distance slid (Fig. 3.13a). But with distance the changes take place in the contacting surface even at same load and sliding velocity. Due to deformation of asperities and creation of valleys with removal of material, the surface gets deteriorated, which is evident from line analysis and 3D-profilometer images at 600 m and 3000 m (Fig. 3.18a-b). The corresponding R_a values 0.532 and 1.030 μm are also shown in the figure. However, coefficient of friction fluctuates within a range of ±0.025 (Fig. 3.13b) which is largely dominated by the presence of hard particles [Gautam and Mohan, 2016; Gautam et al., 2016a, 2016c].

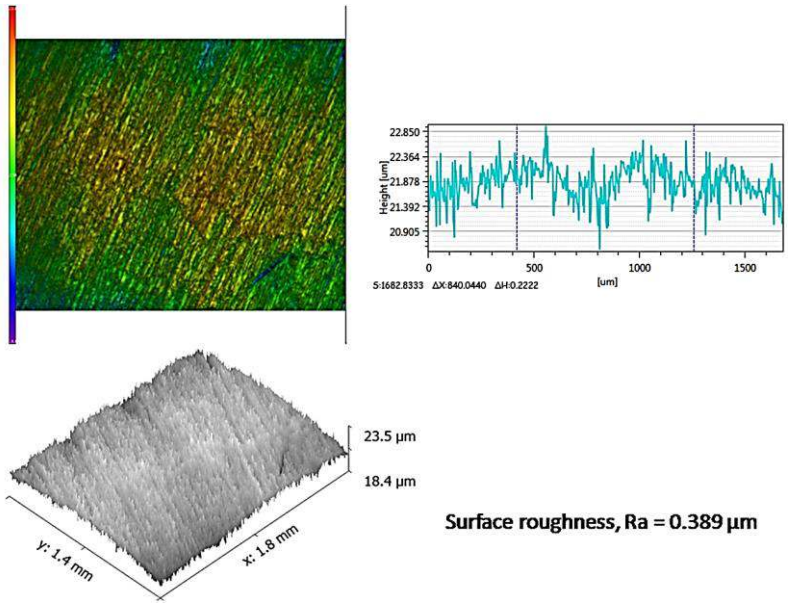

Figure 3.17 – Line analysis and its 3D-profilometry images for composite before wear test.

Aluminium and aluminium alloys are very prone to surface oxidation even at room temperature, hence, an oxide layer is present even at low loads which restricts the direct metal to metal contact of materials in sliding contact. As the normal load increases, the rate of surface deformation increases, cracks are generated in the oxide layer and oxide particles are detached from the surface leading to third body wear. Under such conditions goughing of the surface takes place creating deep grooves and wear nature changes from mild to severe, resulting in a sharp increase in wear rate and wear rate/vol.% Al_3Zr (Fig. 3.14a-b) at high load. Corresponding SEM micrographs of wear tracks in Fig. 3.19a-b show comparatively smooth oxide layer at low load (20 N) and broken oxide layer at high load (40 N), and respective EDS show presence of oxide at low loads and Al_3Zr particles in debris at high loads contributing to severe wear. Iron pick-up has also been observed in few cases and the wear of steel disc was also monitored, but the amount is very little as compared to pin specimens. Presence of oxide indicates mild/oxidative mode of wear and presence of Al_3Zr indicates typical characteristic of severe/oxidative-metallic mode of wear. It is further confirmed by line

analysis and 3D- Profilometer images (Fig. 3.20a-b). The low R_a value of 1.98 µm at low load indicates mild/oxidative wear while high R_a value of 4.00 µm at high load is indicative of oxidative-metallic/severe wear with excessive ploughing of the surface [Gautam and Mohan, 2016; Gautam et al., 2016a, 2016c].

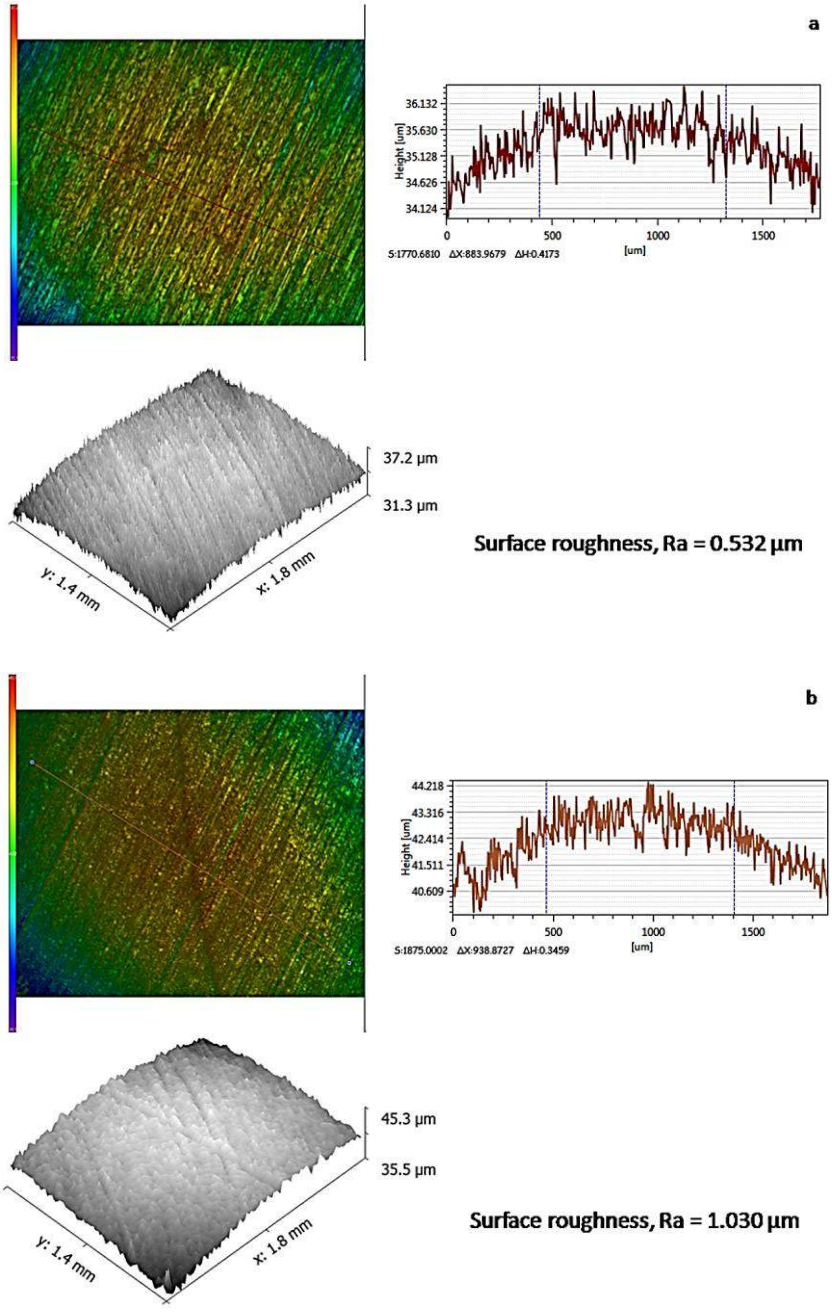

Figure 3.18 – Line analysis and 3D-profilometry images for composite with 10 vol.% Al_3Zr at 10 N normal load and 1 m/s sliding velocity for a sliding distance of (a) 600 m and (b) 3000 m.

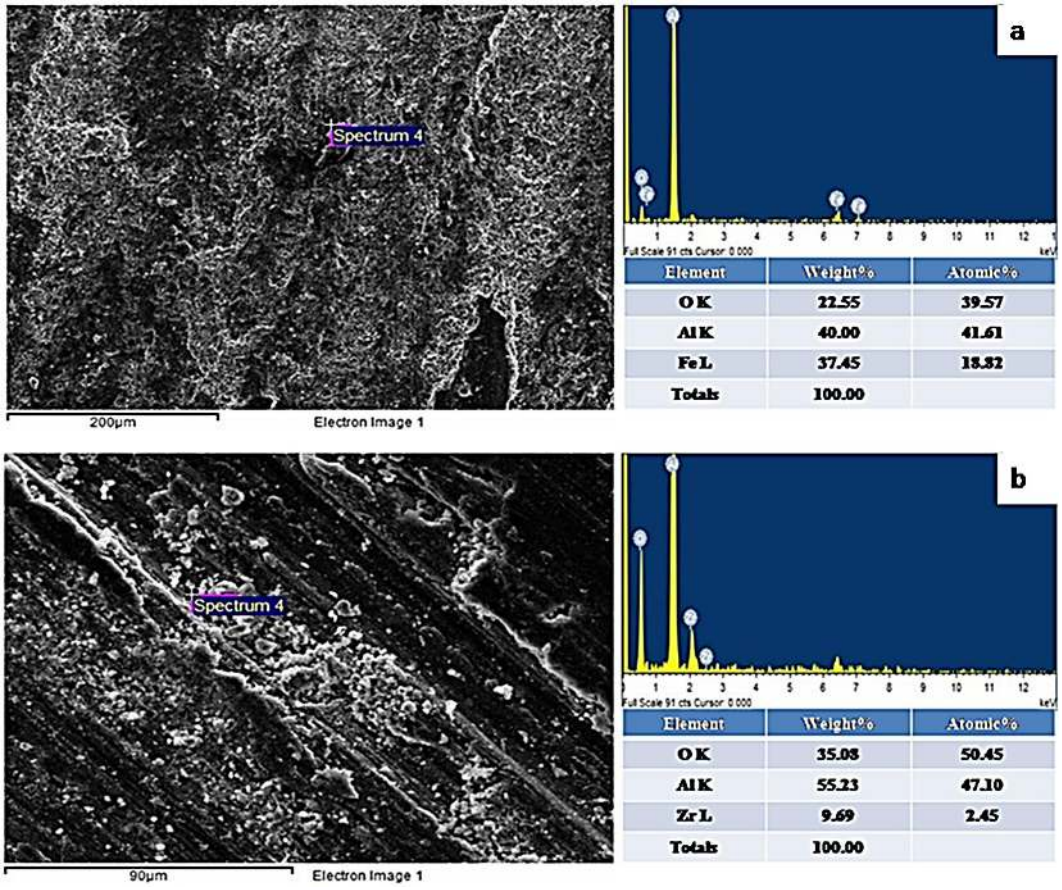

Figure 3.19 – SEM micrographs and corresponding EDS of the wear track with the presence of debris particles in composite with 10 vol.% Al_3Zr at 1 m/s sliding velocity and load of (a) 20 N, and (b) 40 N.

Coefficient of friction decreases with load for all compositions (Fig. 3.14c) which seems to be unusual. But it is important to note that the aluminium-rich phase is much softer as compared to hard Al_3Zr particles, hence, these hard particles largely contribute to the coefficient of friction. During the sliding process these particles are either ploughed away or entrapped within the base material and coefficient of friction decreases. The actual contact area depends on the surface condition. In smooth surfaces actual area of contact is much larger as compared to rough surfaces. In the present case among all contributory factors (Asperity deformation, adhesion, ploughing and third body) to COF [Mohan and Mohan, 2015], contribution of third body is largest due to the presence of hard particles. But as the load increases this contribution gets subsided

due to merging of these hard particles in the soft matrix but ploughing component increases as evident from roughness values. Though roughness values are higher but due to merging of Al_3Zr particles, contribution made by these particles gets minimized (which contributes in a larger way as compared to rest of three) and overall COF decreases (Fig. 3.14c) [Gautam and Mohan, 2016; Gautam et al., 2016a, 2016c].

With increase in sliding velocity the temperature of the contacting surface increases and oxidation becomes more pronounced covering the larger surface area. As a result, both wear rate and wear coefficient decrease and reach a minimum value at 3 m/s sliding velocity for base alloy and composites with 10, 12.5, and 15 vol.% Al_3Zr. But as the velocity is increased further thick oxide layer breaks and contributes as third body wear, thereby wear rate and wear coefficient increase sharply (Fig. 3.15a-b). SEM results shown in Fig. 3.21a-b are in agreement showing smooth surface at low sliding velocity (Fig. 3.21a) and highly distorted surface at high sliding velocity (Fig. 3.21b). The EDS analysis is also in agreement with results (Fig. 3.22a-b). Line analysis and 3D-Profilometer image also show less distortion of the surface at 2 m/s sliding velocity with R_a value of 1.35 μm as compared to severely distorted surface at high velocity of 4 m/s with R_a value of 4.85 μm (Fig. 3.23a-b) [Gautam and Mohan, 2016; Gautam et al., 2016a, 2016c].

However, with higher compositions of 20 and 30 vol.% Al_3Zr particles in composites, presence of intermetallic particles plays a crucial role in deciding the overall wear. Al_3Zr particles may either come out of the surface or merge within the softer matrix. So even at moderate or intermediate velocity slightly higher wear rate and wear coefficient are observed, but at high sliding velocity wear rate and wear coefficient of above

mentioned compositions are marginally less as compared to base alloy and composites with 10, 12.5, and 15 vol.% Al_3Zr. It is also evident from line analysis and 3D-Profilometer study which shows R_a values of 2.74 and 3.95 µm at 2 and 4 m/s sliding velocities respectively for composite with 30 vol.% Al_3Zr (Fig. 3.24a-b). This suggests that composites with higher amount of Al_3Zr particles can be successfully used at comparatively higher sliding velocities.

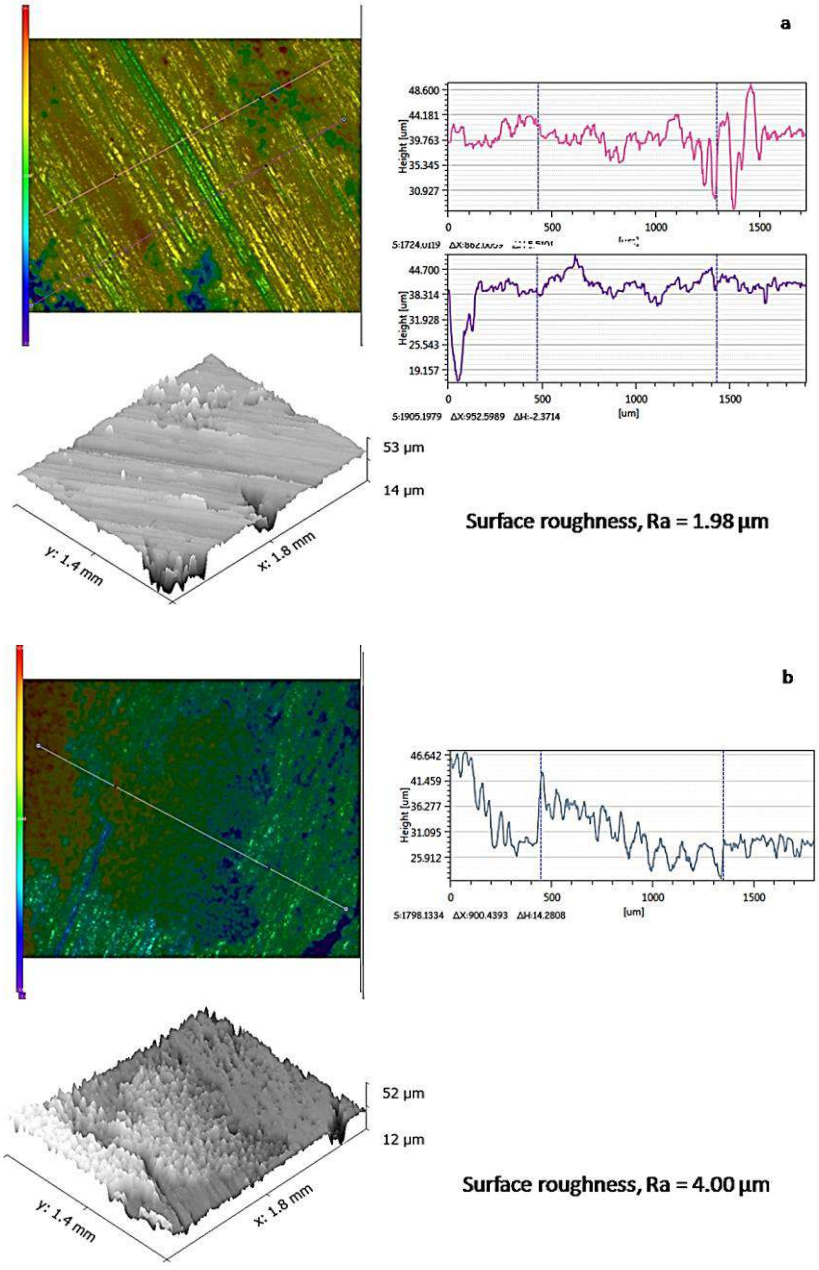

Figure 3.20 – Line analysis and 3D-profilometry images for composite with 30 vol.% Al_3Zr at 1 m/s sliding velocity and normal load of (a) 30 N, and (b) 40 N.

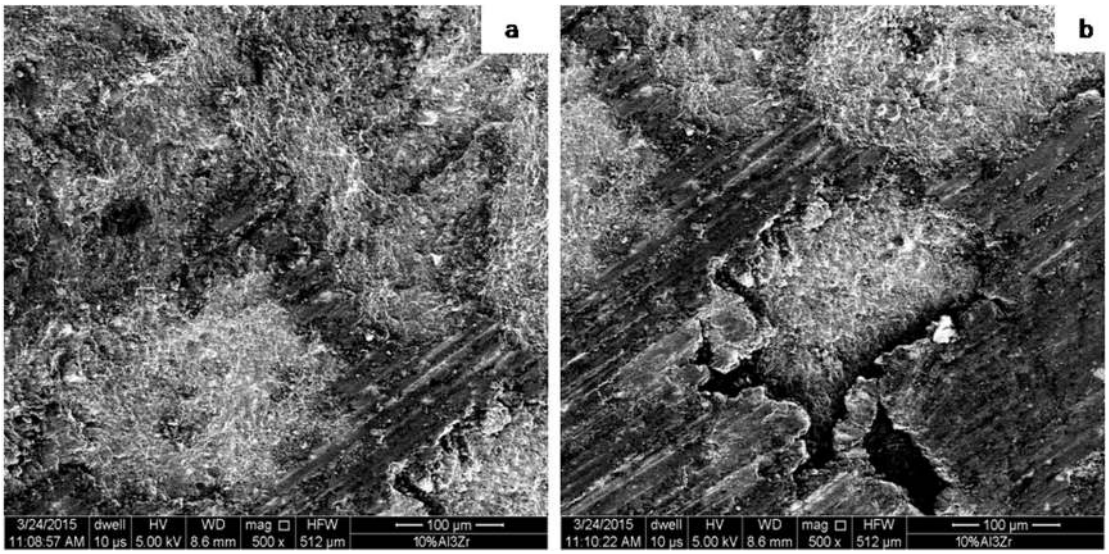

Figure 3.21 – The SEM micrographs of wear track for composite with 10 vol.% Al_3Zr at 20 N normal load and sliding speed of (a) 1 m/s, and (b) 4 m/s.

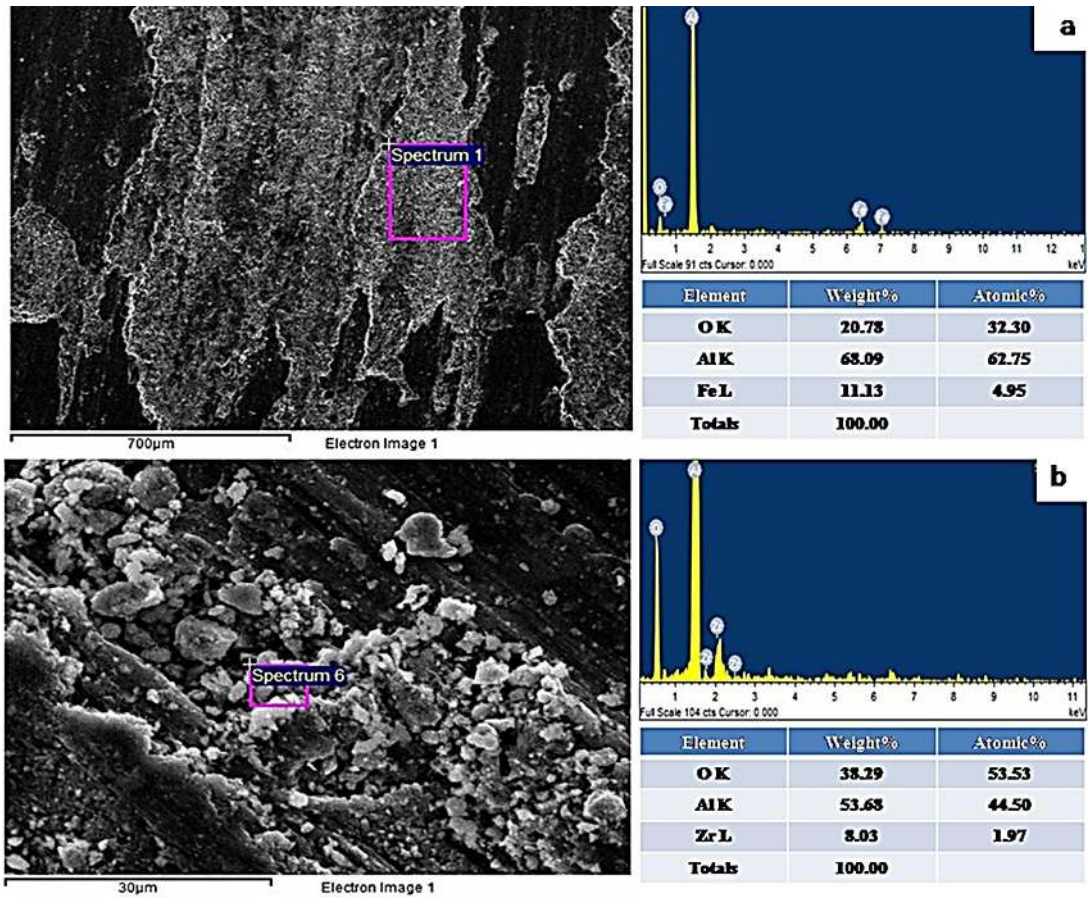

Figure 3.22 – The SEM micrographs and their corresponding EDS pattern of wear track for composite with 10 vol.% Al_3Zr at 20 N normal load and sliding speed of (a) 2 m/s, and (b) 4 m/s.

The coefficient of friction continuously increases with increase in sliding velocity for all the composites and Al-Mg alloy (Fig. 3.15c). Due to the increase in the amount of hard oxide particles coefficient of friction increases. Situations faced in different applications decide the combination of properties so either we want different material or we want materials to act differently. With increase in sliding velocity surface hardening takes place due to the formation of hard oxide layer. Apart from hard Al_3Zr particles, hard oxide also contributes to COF. Though on the other side it restricts metal to metal contact and reduces wear. After certain sliding velocity hard oxide film breaks which further contributes to COF as third body effect [Gautam and Mohan, 2016; Gautam et al., 2016a, 2016c].

Al_3Zr vol.% also affects the wear rate, normalised wear rate and wear coefficient (Fig. 3.16a-c), they show a decreasing trend with increasing vol.% of Al_3Zr particles. The *insitu* formation of Al_3Zr particles refines the Al-rich matrix (Fig. 3.5). Orowan strengthening and increase in dislocation density improves overall strength and hardness (Table 3.7) of composites and this phenomenon is pronounced at higher vol.% of Al_3Zr particles. Hence, all three parameters i.e. wear rate, normalised wear rate and wear coefficient decrease with increase in hardness following Archard's law [Archard, 1953]. Line analysis and 3D-Profilometer image of the wear tracks also indicate a decrease in R_a value, i.e. 2.30, 1.82 and 1.60 μm (Fig. 3.25a-c) for base alloy and composites with 10 & 30 vol.% of Al_3Zr particles respectively under same conditions of load and sliding velocity [Gautam and Mohan, 2016; Gautam et al., 2016a, 2016c].

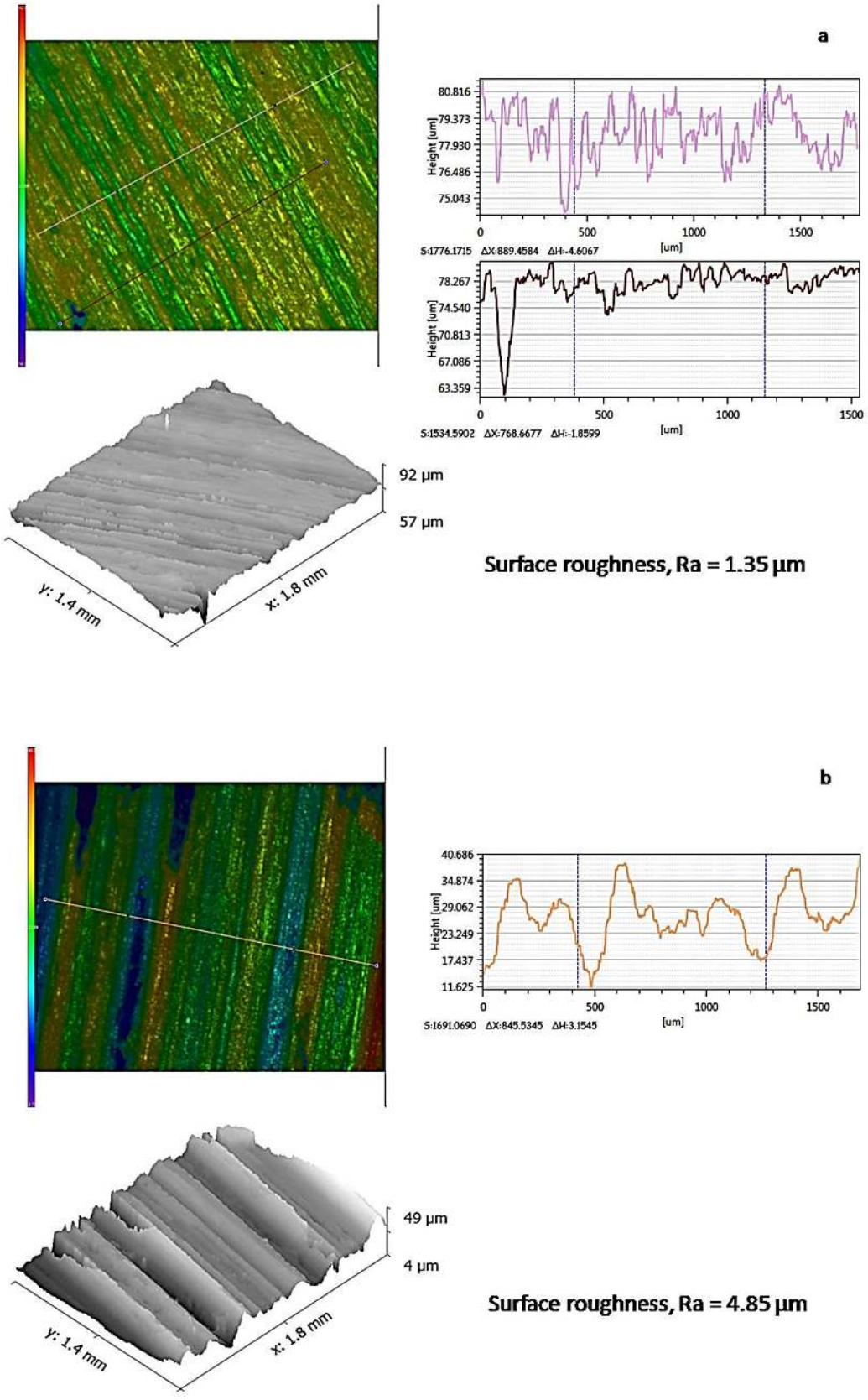

Figure 3.23 – Line analysis and 3D-profilometer images for composite with 10 vol.% Al_3Zr at 20 N load and sliding velocity of (a) 2 m/s, and (b) 4 m/s.

Further, retention of hard particles in the soft Al-rich phase contributes to coefficient of friction and it increases with increasing vol.% of Al_3Zr particles (Fig. 3.16d). Debris analysis (Fig. 3.19a-b) also supports these results showing the presence of aluminium oxide at low loads and sliding velocities and aluminium, aluminium oxide & Al_3Zr at high loads and high sliding velocities. This is clear indication of mild/oxidative wear at lower operating parameters and severe/oxidative-metallic wear at higher operating parameters. Mohan et al. [2008] also observed the same phenomenon in case of Al-Cu-Pb composites. High wear resistance and COF with increasing amount of Al_3Zr indicate that it could be a suitable brake material. In general, hard particles are dispersed in a softer matrix which are the main cause of higher coefficient of friction. Overall COF is the contribution of four components (asperity deformation, adhesion, ploughing and third body) [Mohan and Mohan, 2015]. In case of composites presence of hard particles increases the ploughing component as compared to alloys. Further, fourth component (third body) comes due to hard particles which is more likely in case of composites. Hence, overall COF is higher in composites [Gautam and Mohan, 2016; Gautam et al., 2016a, 2016c].

3.9 Coefficient of Linear Thermal Expansion

Table 3.8 shows the theoretical coefficient of linear and volumetric thermal expansion of all compositions. A decreasing trend is observed with increasing amount of Al_3Zr particles in the Al-Mg alloy composites. It is due to the fact that Al_3Zr phase has low coefficient of thermal expansion as compared to Al-Mg alloy. Coefficient of linear thermal expansion is an important parameter when materials are used at high temperature applications [Gautam et al., 2016c].

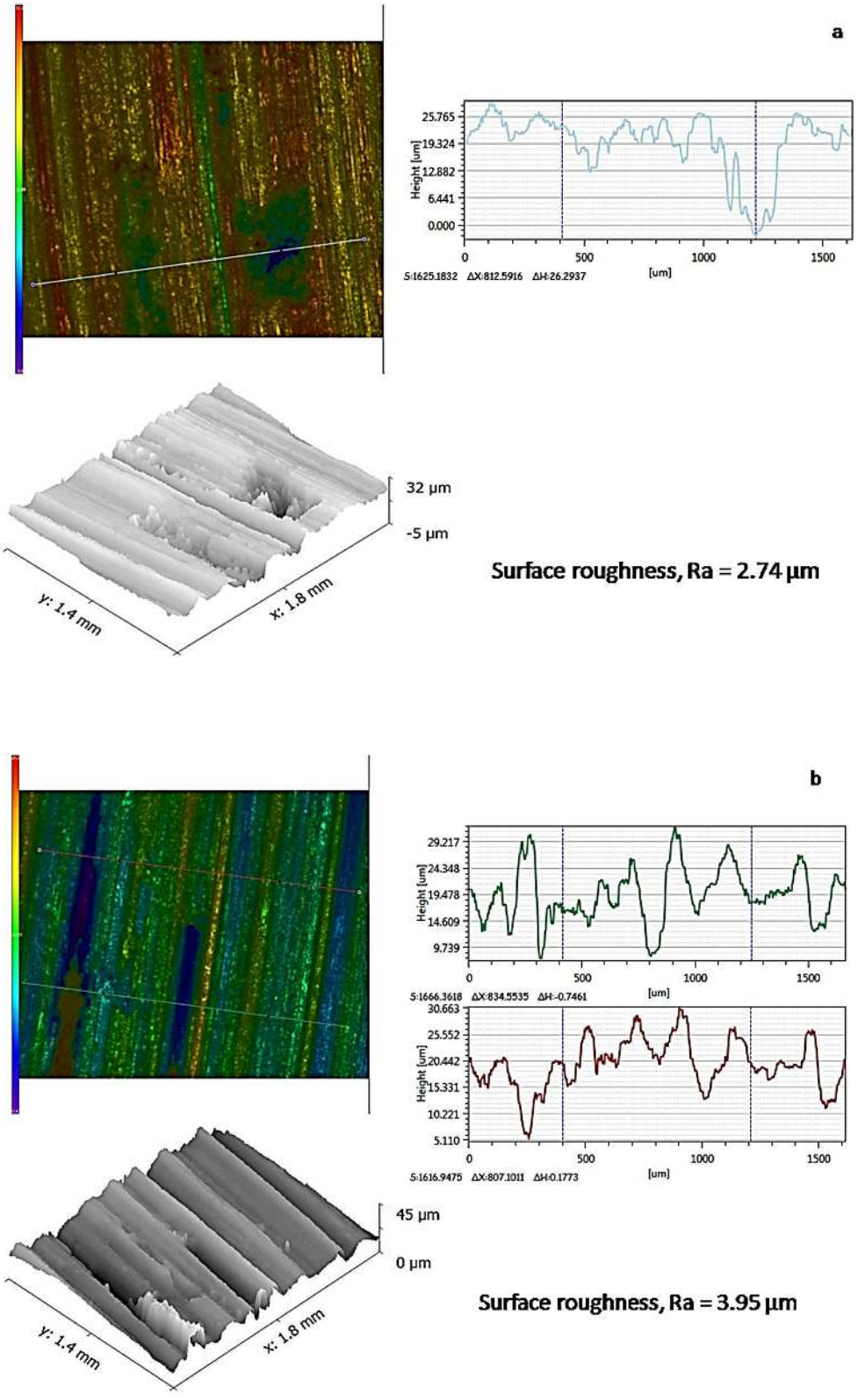

Figure 3.24 – Line analysis and 3D-profilometer images for composite with 30 vol.% Al_3Zr at 20 N load and sliding velocity of (a) 2 m/s, and (b) 4 m/s.

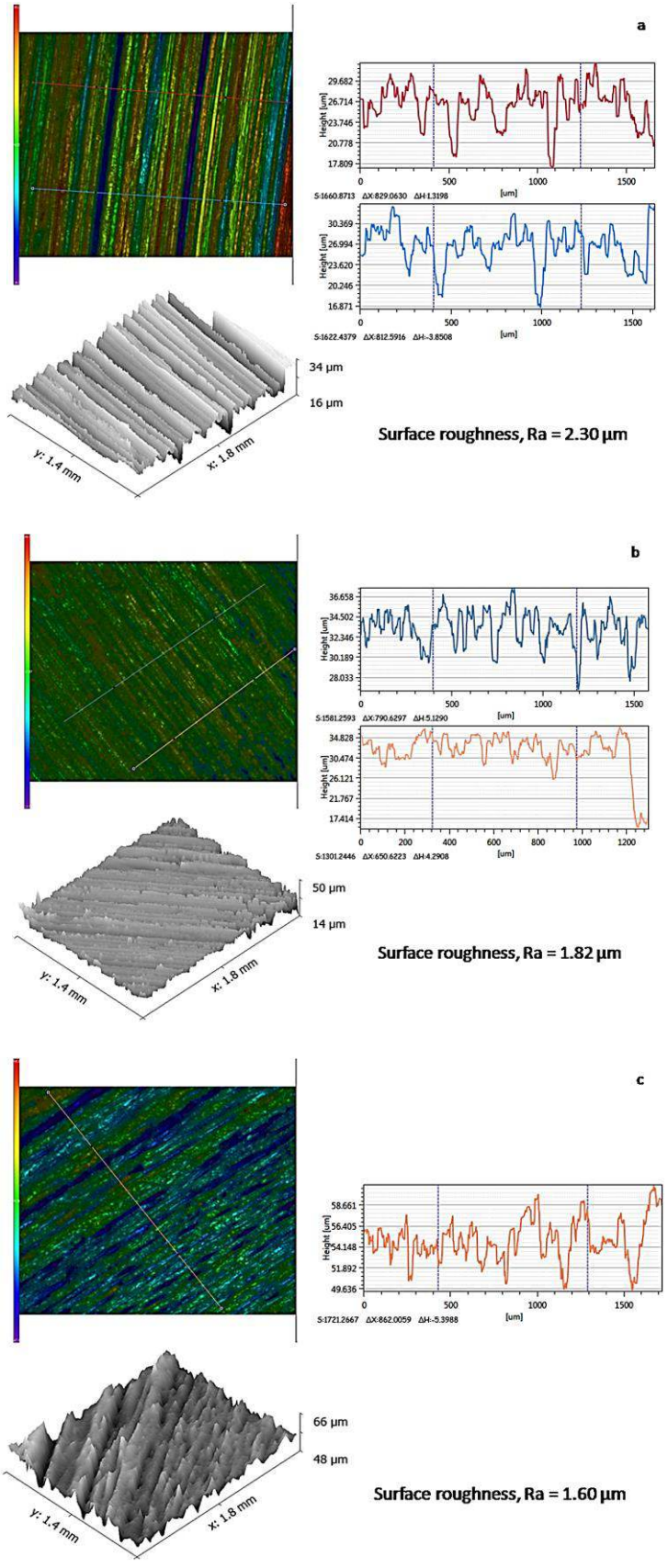

Figure 3.25 – Line analysis and 3D-profilometer images at 20 N load and 1 m/s sliding velocity for (a) Al-Mg alloy, (b) composite with 10 vol.% Al_3Zr, and (c) composite with 30 vol.% Al_3Zr.

Table 3.8 – Coefficient of linear and volumetric thermal expansion for all compositions.

Materials	**Theoretical Coefficient of linear thermal expansion (x 10^{-6} m/m K)**	**Coefficient of volumetric thermal expansion (β= 3α) (x 10^{-6} m/m K)**
Al-Mg alloy	23.80	71.4
10 vol.% Al_3Zr	22.21	66.63
12.5 vol.% Al_3Zr	21.83	65.50
15 vol.% Al_3Zr	21.46	64.39
20 vol.% Al_3Zr	20.74	62.22
30 vol.% Al_3Zr	19.38	58.14

3.10 Conclusions

Following conclusions have been drawn from the present study:

1. XRD and EDS analysis confirm that Al_3Zr particles reinforced Al-Mg alloy *insitu* composite can be successfully synthesized by direct melt reaction (DMR) technique using K_2ZrF_6 inorganic salt and Al-Mg alloy.
2. Density of the composites increases with increasing vol.% of Al_3Zr particles. Porosity is within in a limit of 5 to 7 %.
3. The average grain size of the matrix reduces with *insitu* formed Al_3Zr particles.
4. Mostly polyhedron and rectangular Al_3Zr particles in a size range of 5 – 19 μm are present, however, few rod like particles with BCT structure are also observed.
5. UTS and YS of Al-Mg alloy improved with incorporation of Al_3Zr up to 15 vol.% of Al_3Zr, but with further increase in the amount of Al_3Zr particles in the

composites these properties are adversely affected. However, hardness continuously improves.

6. % elongation improved with 10 vol.% of Al_3Zr particles but decreased with further addition of Al_3Zr particles in the composites.

7. Cumulative mass loss shows a linear relationship with sliding distance but surface gets deteriorated with distance.

8. Wear rate and wear rate/vol.% of Al_3Zr particles increase continuously with increase in applied load. Transition from mild to severe wear takes place above 30 N load, however, composites with high vol.% Al_3Zr can be used even at higher loads due to less wear rate.

9. Wear rate and wear coefficient show a decreasing trend up to 3 m/s sliding velocity and remain in mild wear regime, and beyond this velocity severe wear is observed. However, in composites with 20 and 30 vol.% Al_3Zr, both wear rate and wear coefficient increase continuously but wear rate at 4 m/s sliding velocity is much less as compared to base alloy and composites with 10, 12.5 and 15 vol.% Al_3Zr, which indicates that these composites can be used at high sliding velocities.

10. Wear rate, normalized wear rate and wear coefficient all decrease continuously with increase in vol.% of Al_3Zr particles.

11. Coefficient of friction shows increasing trend with an increase in sliding velocity and composition, however, with increasing load the coefficient of friction decreases.

12. Debris analysis shows two modes of wear i.e. mild/oxidative at low loads and sliding velocities, and severe/oxidative-metallic at high loads and sliding velocities.

13. 3D-Profilometer images, line analysis, R_a values, and SEM studies of worn surfaces all are in agreement with wear results.

14. Low wear rate and high coefficient of friction indicate that it could be a suitable brake material.